ADVANCED MATERIALS
www.advmat.de

www.MaterialsViews.com

Probing Interfacial Electronic Structures in Atomic Layer $LaMnO_3$ and $SrTiO_3$ Superlattices

By *Amish B. Shah, Quentin M. Ramasse, Xiaofang Zhai, Jian Guo Wen, Steve J. May, Ivan Petrov, Anand Bhattacharya, Peter Abbamonte, James N. Eckstein,* and *Jian-Min Zuo**

An epitaxial interface between two strongly correlated transition metal oxides can lead to emergent electronic states at the interface, because the explicit breaking of translational symmetry can nucleate new electronic phases.[1–4] Recent studies have shown that new interfacial states in oxides can be designed and constructed using physical vapor deposition techniques (for a review, see Reference [5]), and when the interface is repeated in close spacing (~a few unit cells), it can lead to bulk-like properties.[6,7] Some interfaces that have attracted considerable attention recently are those formed between two perovskites of $LaTiO_3$ and $SrTiO_3$[8] or $LaMnO_3$ and $SrMnO_3$.[6,7,9] These constituents are all insulating individually in the bulk phase. However, the interfaces become highly conductive via different mechanisms; the interface of $LaTiO_3$-$SrTiO_3$ has layer-to-layer charge transfer[10,11] and the interface of $LaMnO_3$-$SrMnO_3$ is between two antiferromagnetic insulators.[6,9,12] Some strongly correlated perovskites also exhibit competing orders involving charge and spin, resulting in a heightened sensitivity to temperature, external fields, and strain.[13] By combining different perovskites in an epitaxial superlattice, the interruption of translational lattice symmetry and strain can be used to favor one competing order over others.

Growing atomically sharp interfaces and controlling the stoichiometry and defects have been shown to be critical for achieving desired interfacial properties.[1,14–18] Atomic resolution characterization is essential to determine the interface structure and to map interfacial electronic states. This can be achieved by electron energy loss spectroscopy (EELS) in combination with atomic resolution scanning transmission electron microscopy (STEM) using an annular dark-field (ADF) detector.[19] Here, we report the interfacial electronic structure characterization of a $m \times (LaMnO_3)/n \times (SrTiO_3)$ superlattice based on aberration-corrected STEM and EELS. This superlattice was designed to enhance the optical absorption using interfacial states by contacting a band insulator, $SrTiO_3$ (STO), with a Mott-insulator $LaMnO_3$ (LMO).[20] This system is also interesting because of the presence of $La_{1-x}Sr_xMnO_3$-$SrTiO_3$ and $Sr_{1-x}La_xTiO_3$-$LaMnO_3$ interfaces shown in the layering model of Figure 1a. $La_{1-x}Sr_xMnO_3$ in bulk phase is a spin-polarized and ferromagnetic and has received considerable attention recently for spin-valve applications.[21] La doping makes $Sr_{1-x}La_xTiO_3$ metallic for x as small as <0.1[22] and superconducting. We have grown a 2×2 superlattice with $m = n = 2$ over a large thickness of 63 ± 1 layers of LMO and STO. The structure consists of one unit

[*] Prof. J. M. Zuo, A. B. Shah
Department of Materials Science and Engineering and Fredrick Seitz Materials Research Laboratory University of Illinois at Urbana-Champaign
Urbana, Illinois 61801, USA
E-mail: jianzuo@illinois.edu

Dr. Q. M. Ramasse
National Center for Electron Microscopy
Lawrence-Berkeley National Laboratory
Berkeley, CA 94720 USA

Dr. X. Zhai, Prof. P. Abbamonte, Prof. J. N. Eckstein
Department of Physics and Fredrick Seitz Materials Research Laboratory
University of Illinois at Urbana-Champaign
Urbana, Illinois, 61801, USA

Dr. J. G. Wen, Dr. I. Petrov
Fredrick Seitz Materials Research Laboratory
University of Illinois at Urbana-Champaign
Urbana, Illinois, 61801, USA

Dr. S. J. May, Dr. A. Bhattacharya
Materials Science Division and Center for Nanoscale Materials,
Argonne National Laboratory,
Argonne, Illinois 60439, USA

DOI: 10.1002/adma.200904198

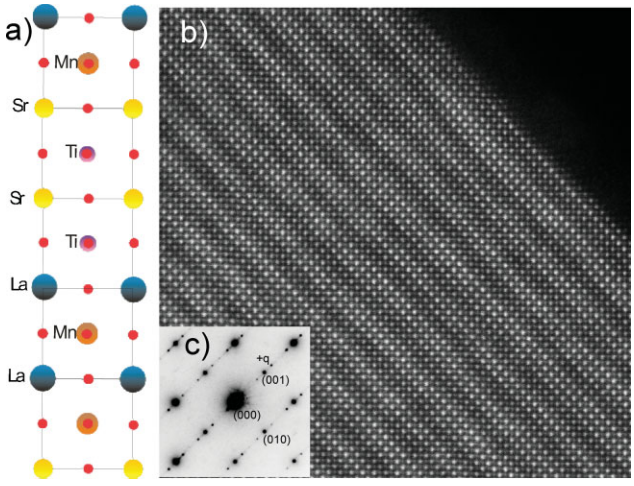

Figure 1. The atomic structure of an oxide superlattice characterized by electron imaging and diffraction. a) A model of the $2 \times LaMnO_3/2 \times SrTiO_3$ superlattice. b) A HAADF-STEM image shows atomic level sharpness of films c) Nanoarea electron diffraction pattern shows the strong fundamental reflections and weak satellite reflections (q) from the superlattice.

cell each of LMO, $La_{0.5}Sr_{0.5}MnO_3$, STO and $Sr_{0.5}La_{0.5}TiO_3$. The small repeating 2×2 supercell and change of both cations on the *A* sites (La and Sr) and *B* sites (Mn and Ti) in the perovskite structure make this superlattice particularly challenging for both synthesis and characterization. The aberration corrected STEM allows EELS core loss fine structure to be analyzed on an atomic scale.

We use the atomic layer-by-layer MBE (ALL-MBE) technique to grow the oxide superlattice. Past studies have shown the ALL-MBE can be used to grow oxide thin-films with 10^{-2} unit cell precision in composition, and making use of beam flux gradients to provide a range of integrated doses, regions in a sample with 10^{-3} unit cell precision can be identified.[23] Details for growth are presented in the paper by Zhai, Eckstein, and collaborators in this issue. The growth was started by depositing first 6 layers of STO as a buffer layer, followed by the growth of superlattice. The growth after the first 3 supercells remained periodic for the remainder of the growth. Figure 1b displays a HAADF STEM image of the upper supercells of the superlattice, which shows that epitixial growth of the films was carried out with atomic sharpness. The superlattice structure was quantified using nanoarea electron diffraction.[24] An example of the superlattice nanoarea electron diffraction pattern is shown in Figure 1c. A diffraction pattern was also recorded from the STO substrate near the superlattice (not shown) and used for calibration. The diffraction spot indexed as (001) is the film growth direction. Weak first order superlattice reflections ($\pm q$) along (001) are clear in the pattern. Using the calibration obtained from the STO substrate, we measured the c-axis length of the average perovskite cell in the superlattice from Figure 1c and obtained $\overline{c}_{SL} = 3.92$ Å. The *c*-axis is elongated by 0.4% compared to the STO substrate. The distance of the first order reflection, q, is measured at 0.237. An ideal 2×2 superlattice should have $q = 0.25$. Thus, for this particular sample, there is a deviation of −5.2%, corresponding to an incommensurate lattice of mixed 2 to 3 unit cells with an averaged repeat of 4.2 times the perovskite unit cell.

The high spatial resolution of EELS allows us to examine the Ti and Mn $L_{2,3}$ edges of individual atomic columns. Figure 2a shows an EELS line scan background subtracted with an exponential law across eight supercells. The integrated edge intensity is plotted in Figure 2b and 2c for Ti and Mn $L_{2,3}$ edges respectively. In each profile, sites where the integrated edge intensity is near the maximum are identified as predominantly Ti or Mn sites and labeled as 1 and 2, respectively. Sites where there are significant mixed Ti and Mn signals are identified as 3. Figure 2d plots the Ti $L_{2,3}$ edges obtained from the three sites. For comparison, the Ti $L_{2,3}$ edge obtained from a separate linescan over the STO substrate is also plotted. Its energy loss axis was shifted so the edge onsets are at the same value for comparison. The spectra are normalized above the edge threshold in the energy window between 470 and 490 eV. Ti sites 1 and 2 in the superlattice show similar near edge structure. However, these Ti $L_{2,3}$ edges are different from that of the substrate. The Ti spectra from the superlattice have slightly more intensity between the t_{2g} and e_g peaks for both the L_2 and L_3 edges, while the spectra from the substrate has a sharper drop in the minimum between these peaks. The difference is not caused by a change in EELS energy resolution; both spectra were obtained with the same instrument setting. This will be further discussed next together with

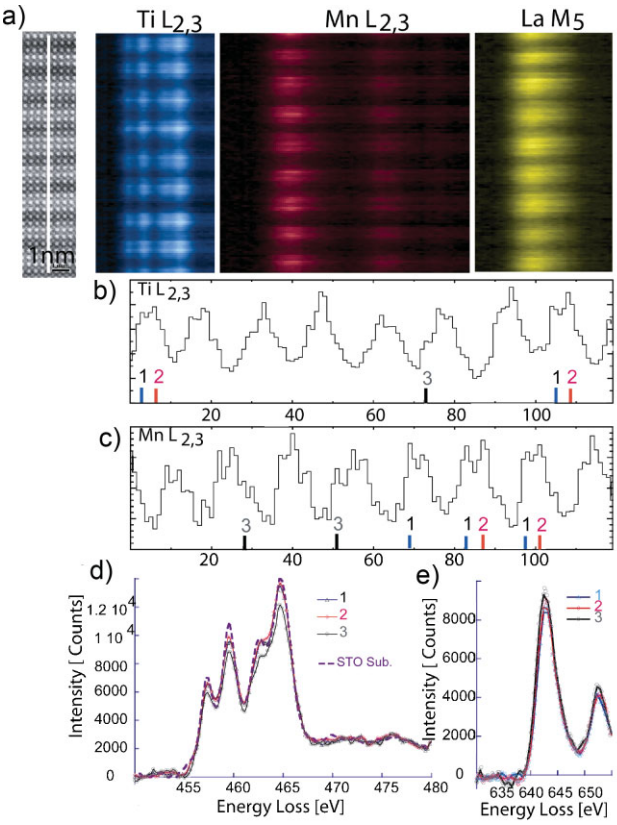

Figure 2. Atomic scale mapping ELNES of Ti and Mn $L_{2,3}$ edges. a) The HAADF-STEM image marked with the position of the EELS line scan and EELS spectral maps for Ti and Mn $L_{2,3}$ edges and La M_5. b) The integrated edge intensity of the Ti $L_{2,3}$ used to identify sites 1 and 2, which have little or no Mn mixing, and site 3 with significant Mn mixing. c) Similarly, the integrated edge intensity of the Mn $L_{2,3}$ used sites 1 and 2 with little or no Ti mixing, and site 3 with Ti mixing. d,e) Averaged spectra obtained from the sites identified in b) and c).

evidences from the O *K* edge. The Ti $L_{2,3}$ edges obtained from site 3 have a smaller intensity and the same ELNES features as the other two sites. The comparison for two different Mn atomic columns is shown in Figure 1e, which is normalized to the minimum between the L_3 and L_2 peaks. Mn sites 1 and 2 give similar ELNES. A noticeable difference is observed in the spectrum obtained from site 3 characterized by a larger increase in L_3 edge peak than the L_2 edge. The change in the L_3/L_2 ratio in Mn oxides, in general, indicates a change in the oxidation state.[25,26]

The chemical structure that we concluded from the EELS data of Figure 2a and HAADF-STEM images is shown schematically in Figure 3a. There are two different Mn and Ti sites respectively in the superlattice with Ti2 and Mn2 between LaO and SrO atomic layers. In the simple ionic picture with La and Mn as 3+, Ti as 4+ cations, and O as 2- anion, the superlattice is neutral and there is a dipole across 2.5 unit cells between the LaO atomic layer above the Ti2 and MnO_2 atomic layer of the Mn2 site. To look for possible effect of this dipole, we examined the O *K* edges inside the superlattice and in the STO substrate. The O *K* edge has been shown to be sensitive to the electronic structure in oxide superlattices.[27,28] However, in these previous studies, the EELS

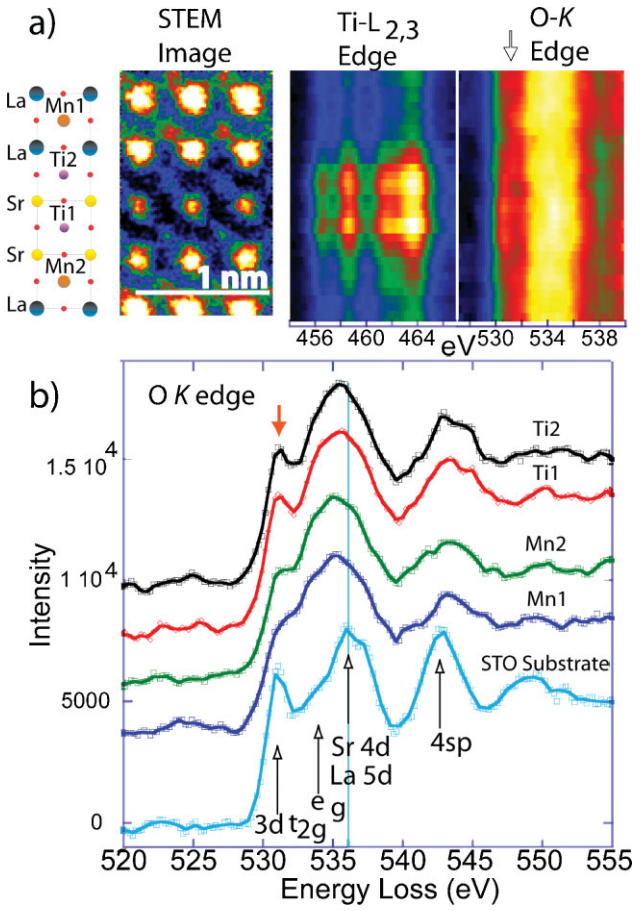

Figure 3. The mapping of O *K* edge for Ti and Mn atomic columns inside the superlattice. a) the O *K* edge map from a line across a single supercell of the superlattice. The map is shown together with a structural model of the superlattice, the HAADF-STEM image and the Ti $L_{2,3}$ edges obtained in the same line scan. The spectral maps were background subtracted with an exponential fit. b) O *K* edge spectra on four different atomic sites, Ti1, Ti2, Mn1 and Mn2, as labeled in a). An averaged O *K* edge spectrum obtained from the $SrTiO_3$ substrate is also shown for reference. The down arrows point to the prepeak of the O *K* edge as discussed in text.

spatial resolution was not high enough to examine the O *K* edge on an individual unit cell basis. In this study, the spatial resolution of EELS is significantly improved with aberration correction as evidenced by the above Ti and Mn L edge data.

Figure 3 examines the ELNES of the O *K* edge that is mapped within the length of a superlattice unit cell. The HAADF-STEM image and the Ti $L_{2,3}$ edges are shown together with the O *K* edge in Figure 3a. The position of the O *K* prepeak in the EELS line scan is indicated by the downward arrow. Figure 3b plots the EELS spectrum of O *K* edge obtained on the Ti1, Ti2, Mn1 and Mn2 *B*-sites as illustrated in Figure 3a. The spectrum plotted is an average of 3 to 4 spectra on each *B*-site. The spectra were background subtracted using an exponential law. For comparison, we also plotted in Figure 3b an averaged spectrum from the STO substrate, which was obtained in a separate line scan. The energy scale was shifted so the onsets meet at the same position. The O *K* edge originates from the transition from the O *1s* to unoccupied *2p* states. This edge is pushed up to the continuum at higher energy if the *2p* states are fully occupied as for O^{2-} ions. The observed O *K* edge is the result of hybridization between the O *2p* and transition metal states. The main peaks of the O *K* edge can be attributed to the 3d states of the Mn or Ti *B*-site cation, *4d* states of Sr or 5*d* states of La at the *A*-site cation, and *4s* and *4p* of the *B*-site cation as labeled in Figure 3b.[29–31] The relative strength of the prepeak at 531 eV is an indication of *d*-band filling;[31] the peak is strongest in the STO substrate where the *d*-band is largely unoccupied, and the peak is weakest in LMO with its 3*d* t_{2g} band fully occupied in the spin up band. At the interface of between atomic layers of LaO-MnO_2-SrO, we see an increase in the prepeak intensity, similar to the behavior of Sr doping in LMO.[32] The prepeak intensity at Ti1 and Ti2 sites are similar. Both are noticeably weaker than the prepeak in the STO substrate, indicating a lowered number of unoccupied states of Ti *3d* in the t_{2g} band of the superlattice. We also notice a significant peak shift for the second peak of the O *K* edge attributed to the Sr *4d* on all superlattice sites as La *5d* bands mix with Sr *4d* (The e_g peak is not distinctly resolved in the spectra). The spectral shape is similar to what is observed for La doped STO by X-ray absorption spectroscopy.[22]

Figure 4 shows the transition of O *K* edges from the STO substrate to the deposited STO buffer layer to first a few layers of LMO and STO. The HAADF-STEM image marked with the line scan position and the position of the STO buffer layer are shown in Figure 4a and the O *K* edge map is shown in Figure 4b together with Ti $L_{2,3}$, Mn $L_{2,3}$ maps. All spectra were background subtracted with a power law. The O *K* edge map reveals clear changes in the superlattice 1) a shift to lower energy loss for the peak attributed to hybridization of O *2p* with Sr 4*d* or La 5*d*, and 2) a reduction of the prepeak intensity, while the O *K* edge in the STO buffer is the same as the STO substrate. This trend is further explored in Figure 4c, which plots the EELS spectrum of O *K* edge taken from the STO substrate, the STO buffer and the STO layer in the superlattice. The spectrum plotted was an average of 5 spectra in each case. There is no appreciable difference between the overlapped O *K* edge from the STO substrate and the deposited STO buffer layer film. The spectrum from the STO film inside the superlattice (the position is marked in Figure 4b by a white arrow) show similar ELNES features as observed in Figure 3 with broadening in the third peak attributed to O *2p* hybridization with Sr 4d and La 5*d*, a less intense prepeak, and a chemical shift of the edge onset. The overlaid Ti $L_{2,3}$ edges of the buffer layer and STO substrate in Figure 4d also show no appreciable difference while the spectrum from the STO thin film has a slight broadening in the t_{2g}-e_g splitting of the L_2 peak. The difference plotted in Figure 4d is between the superlattice and an average of the STO substrate and STO buffer layer. The same chemical shift toward lower energy loss observed in the O *K* edge is also observed for the Ti $L_{2,3}$ edge. The amount of chemical shift is measured at 0.22 eV, which agrees with the optical absorption spectroscopy data.[20] The EELS results show that the band alignment observed by the optical absorption spectroscopy occurs in STO corresponding to a lowering of the conduction band edge.

The above observed chemical shift of O *K* and Ti $L_{2,3}$ edges and changes in the fine structure O *K* all point to new interfacial electronic structures in the 2 × $LaMnO_3$/2 × $SrTiO_3$ superlattice. The O *K* prepeak shows an increase at the Mn2 sites and a decrease at both Ti sites indicate that the electron from the LaO atomic layer is redistributed in STO and the interfacial Mn2. The

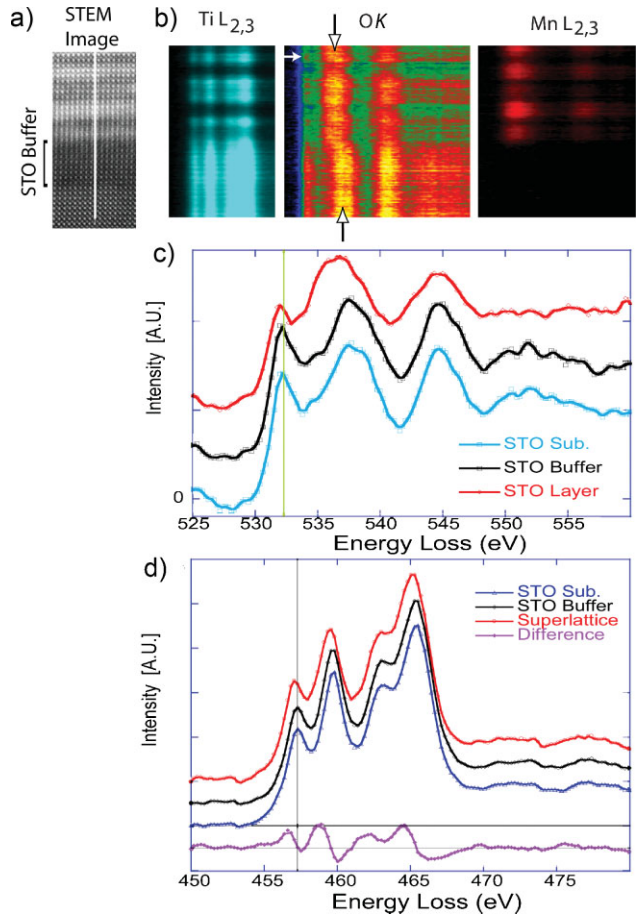

Figure 4. a) HAADF STEM image after a linescan shows the buffer layer of STO indicated by the bracket over the STO substrate. The buffer layer and thin films are slightly misoriented from the substrate. This misorientation disappears in the third supercell. b) EELS spectra background subtracted with a power law fit. The broad peak in the O *K* edge shifts towards lower energy loss in the STO thin films, but not in the STO buffer layer. c) Ti $L_{2,3}$ and O *K* spectra averaged over five integration points from the substrate, buffer layer, and a STO film indicated by the horizontal white arrow.

change we observed in Ti $L_{2,3}$ edge in STO is too small compared to the difference in the fine edge structures that one expects for Ti^{3+} and Ti^{4+} (see Reference [8]). The amount of electron transfer to Ti likely is small, much less than one electron. The predominant change in the O *K* edge within individual unit cells suggests that electron transfer is achieved through the transition metal and oxygen bonding. The small electron transfer into STO observed here is in contrast to a recent EELS study on a 17×LMO/2×STO superlattice,[33] which reported mostly a Ti^{3+} oxidation state in STO. This superlattice has an extra LaO atomic layer, which is not present in our case.

In summary, we have demonstrated direct EELS evidences of interfacial electronic states for band alignment and interfacial electron transfer, or charge leakage, in a $2 \times LaMnO_3/2 \times SrTiO_3$ superlattice. The superlattice is epitaxially strained. The band alignment, in the form of a 0.22 eV chemical shift of O *K* and Ti $L_{2,3}$ edges, was observed in ultrathin STO. The electron transfer from LMO to STO is evidenced by a reduction in the intensity of O *K* edge prepeak in STO, which is attributed to unoccupied O 2p states from hybridization with the Ti 3d t_{2g} states. Electron probe aberration correction was essential for the high spatial resolution mapping of interfacial electronic states.

Experimental

After growth, cross sectional samples for electron microscopy were prepared by mechanical wedge polishing and ion milling. Microscopy was carried out on a 200 kV JEOL JEM2200FS STEM. This microscope is equipped with a CEOS 3rd order probe forming spherical aberration (C_s) corrector to reduce the probe size to ~1 Å.[34] The microscope has been shown to be able to resolve 1.04 Å spacing between two Ga atomic columns viewed along the [120] direction in GaN thin films.[35] To record EELS, the energy dispersion is obtained using an in-column omega-energy filter. For EELS spectroscopy, we used a 26 mrad probe convergence angle and a 41 mrad collection angle. The probe current was measured to be ~165 pA. (The image shown in Figure 1 differs from the other figures in that the semi-convergence angle is 16 mrad and the probe current is ~13 pA). The EELS spectra are background-subtracted with an exponential or power law to remove the contribution of random multiple scattering of electrons through the sample.

Acknowledgements

Research is supported by the U.S. Department of Energy, Division of Materials Sciences under grant DEFG02-91ER45439 and Argonne National Laboratory under the U.S. Department of Energy grant DE-AC02-06CH11357 Digital Synthesis FWP. Microscopy was carried out at the Frederick Seitz Materials Research Laboratory Central Facilities, University of Illinois, which is partially supported by the U.S. Department of Energy under grants DE-FG02-07ER46453 and DE-FG02-07ER46471, and the National Center for Electron Microscopy, Lawrence Berkeley Lab, which is supported by the U.S. Department of Energy under grant DE-AC02-05CH11231. JMZ thanks Dr. Maria Varela for sharing a preprint of *Advanced Materials* and helpful discussions.

Received: December 8, 2009
Published online: February 10, 2010

[1] S. Okamoto, A. J. Millis, *Nature* **2004**, *428*, 630.
[2] N. Reyren, S. Thiel, A. D. Caviglia, L. F. Kourkoutis, G. Hammerl, C. Richter, C. W. Schneider, T. Kopp, A. S. Ruetschi, D. Jaccard, M. Gabay, D. A. Muller, J. M. Triscone, J. Mannhart, *Science* **2007**, *317*, 1196.
[3] R. Pentcheva, W. E. Pickett, *Phys. Rev. Lett.* **2007**, *99*, 016802.
[4] B. R. K. Nanda, S. Satpathy, *Phys. Rev. B* **2009**, *79*, 054428.
[5] D. G. Schlom, L. Q. Chen, X. Q. Pan, A. Schmehl, M. A. Zurbuchen, *J. Am. Ceram. Soc.* **2008**, *91*, 2429.
[6] A. Bhattacharya, S. J. May, S. Velthuis, M. Warusawithana, X. Zhai, B. Jiang, J. M. Zuo, M. R. Fitzsimmons, S. D. Bader, J. N. Eckstein, *Phys. Rev. Lett.* **2008**, *100*, 257203.
[7] S. J. May, A. B. Shah, S. G. E. t, Velthuis, M. R. Fitzsimmons, J. M. Zuo, X. Zhai, J. N. Eckstein, S. D. Bader, A. Bhattacharya, *Phys. Rev. B: Condens. Matter* **2008**, *77*, 174409.
[8] A. Ohtomo, D. A. Muller, J. L. Grazul, H. Y. Hwang, *Nature* **2002**, *419*, 378.
[9] S. Smadici, P. Abbamonte, A. Bhattacharya, X. F. Zhai, B. Jiang, A. Rusydi, J. N. Eckstein, S. D. Bader, J. M. Zuo, *Phys. Rev. Lett.* **2007**, *99*, 196404.
[10] A. Ohtomo, H. Y. Hwang, *Nature* **2004**, *427*, 423.
[11] S. Thiel, G. Hammerl, A. Schmehl, C. W. Schneider, J. Mannhart, *Science* **2006**, *313*, 1942.

[12] C. Adamo, X. Ke, P. Schiffer, A. Soukiassian, M. Warusawithana, L. Maritato, D. G. Schlom, *Appl. Phys. Lett.* **2008**, *92*.
[13] M. B. Salamon, M. Jaime, *Rev. Mod. Phys.* **2001**, *73*, 583.
[14] N. Nakagawa, H. Y. Hwang, D. A. Muller, *Nat. Mater.* **2006**, *5*, 204.
[15] J. Junquera, P. Ghosez, *Nature* **2003**, *422*, 506.
[16] K. S. Takahashi, M. Kawasaki, Y. Tokura, *Appl. Phys. Lett.* **2001**, *79*, 1324.
[17] H. Yamada, Y. Ogawa, Y. Ishii, H. Sato, M. Kawasaki, H. Akoh, Y. Tokura, *Science* **2004**, *305*, 646.
[18] M. Takizawa, H. Wadati, K. Tanaka, M. Hashimoto, T. Yoshida, A. Fujimori, A. Chikamatsu, H. Kumigashira, M. Oshima, K. Shibuya, T. Mihara, T. Ohnishi, M. Lippmaa, M. Kawasaki, H. Koinuma, S. Okamoto, A. J. Millis, *Phys. Rev. Lett.* **2006**, *97*, 057601.
[19] D. A. Muller, L. Kourkoutis, M. Murfitt, J. H. Song, H. Y. Hwang, J. Silcox, N. Dellby, O. L. Krivanek, *Science* **2008**, *319*, 1073.
[20] X. Zhai, C. S. Mohapatra, A. B. Shah, J. M. Zuo, J. N. Eckstein, *Adv. Mater.* **2009**, DOI: 10.1002/adma.200904197.
[21] Y. Suzuki, H. Y. Hwang, S. W. Cheong, R. B. Van Dover, *Appl. Phys. Lett.* **1997**, *71*, 140.
[22] A. Fujimori, I. Hase, M. Nakamura, H. Namatame, Y. Fujishima, Y. Tokura, M. Abbate, F. M. F. Degroot, M. T. Czyzyk, J. C. Fuggle, O. Strebel, F. Lopez, M. Domke, G. Kaindl, *Phys. Rev. B* **1992**, *46*, 9841.
[23] M. P. Warusawithana, E. V. Colla, J. N. Eckstein, M. B. Weissman, *Phys. Rev. Lett.* **2003**, *90*.
[24] J. M. Zuo, M. Gao, J. Tao, B. Q. Li, R. Twesten, I. Petrov, *Microscopy Research and Technique* **2004**, *64*, 347.
[25] D. H. Pearson, C. C. Ahn, B. Fultz, *Phys. Rev. B* **1993**, *47*, 8471.
[26] L. A. J. Garvie, A. J. Craven, *Phys. Chem. Miner.* **1994**, *21*, 191.
[27] J. Verbeeck, O. I. Lebedev, G. Van Tendeloo, B. Mercey, *Phys. Rev. B* **2002**, *66*, 184426.
[28] A. B. Shah, X. Zhai, B. Jiang, J. G. Wen, J. N. Eckstein, J. M. Zuo, *Phys. Rev. B* **2008**, *77*.
[29] F. M. F. Degroot, J. Faber, J. J. M. Michiels, M. T. Czyzyk, M. Abbate, J. C. Fuggle, *Phys. Rev. B* **1993**, *48*, 2074.
[30] R. Brydson, H. Sauer, W. Engel, F. Hofer, *J. Phys.: Condens. Matter* **1992**, *4*, 3429.
[31] Z. L. Zhang, W. Sigle, W. Kurtz, M. Ruhle, *Phys. Rev. B* **2002**, *66*, 214112.
[32] M. Abbate, F. M. F. Degroot, J. C. Fuggle, A. Fujimori, O. Strebel, F. Lopez, M. Domke, G. Kaindl, G. A. Sawatzky, M. Takano, Y. Takeda, H. Eisaki, S. Uchida, *Phys. Rev. B* **1992**, *46*, 4511.
[33] J. Garcia-Barriocanal, F. Y. Bruno, A. Rivera-Calzada, Z. Sefrioui, N. M. Nemes, M. Garcia-Hernández, J. Rubio-Zuazo, G. R. Castro, M. Varela, S. J. Pennycook, C. Leon, J. Santamaria, *Adv. Mater.* **2009**, *21*, 1.
[34] M. Haider, S. Uhlemann, J. Zach, *Ultramicroscopy* **2000**, *81*, 163.
[35] J. G. Wen, J. Mabon, C. Lei, S. Burdin, E. Sammann, I. Petrov, A. B. Shah, V. G. Chobpattana, J. Zhang, K. Ran, J. M. Zuo, S. Mishina, T. Aoki, *submitted* **2009**.